Original Article

Multiscale confocal photoacoustic dermoscopy to evaluate skin health

Haigang Ma[1,2]^, Zhiyang Wang[3], Zhongwen Cheng[3], Guo He[3], Ting Feng[1], Chao Zuo[1], Haixia Qiu[4]

[1]Smart Computational Imaging (SCI) Laboratory, Nanjing University of Science and Technology, Nanjing, China; [2]Shenzhen Research Institute of Northwestern Polytechnical University, Shenzhen, China; [3]MOE Key Laboratory of Laser Life Science & Institute of Laser Life Science, College of Biophotonics, South China Normal University, Guangzhou, China; [4]Department of Laser medicine, the First Medical Center of PLA General Hospital, Beijing, China

Contributions: (I) Conception and design: H Ma, H Qiu; (II) Administrative support: C Zuo, H Qiu; (III) Provision of study materials or patients: H Ma, H Qiu; (IV) Collection and assembly of data: H Ma, Z Wang, G He; (V) Data analysis and interpretation: H Ma, Z Cheng, T Feng; (VI) Manuscript writing: All authors; (VII) Final approval of manuscript: All authors.

Correspondence to: Haigang Ma. Smart Computational Imaging (SCI) Laboratory, Nanjing University of Science and Technology, 200 Xiaoling Wei Street, Nanjing 210094, China. Email: mahaigang@njust.edu.cn; Haixia Qiu. Department of Laser medicine, the First Medical Center of PLA General Hospital, 28 Fuxing Road, Beijing 100853, China. Email: qiuhxref@126.com.

Background: Photoacoustic dermoscopy (PAD) is a promising branch of photoacoustic microscopy (PAM) that can provide a range of functional and morphologic information for clinical assessment and diagnosis of dermatological conditions. However, most PAM setups are unsuitable for clinical dermatology because their single-scale mode and narrow frequency band result in insufficient imaging depth or poor spatiotemporal resolution when visualizing the internal texture of the skin.

Methods: We developed a multiscale confocal photoacoustic dermoscopy (MC-PAD) with a multifunction opto-sono objective that could achieve high quality dermatological imaging. Using the objective to coordinate the spatial resolution and penetration depth, the MC-PAD was used to visualize pathophysiological biomarkers and vascular morphology from the epidermis (EP) to the dermis, which enabled us to quantify skin abnormalities without using exogenous contrast agents for human skin.

Results: The MC-PAD was shown to have the ability to differentiate between different types of cells (such as red blood cells and melanoma cells), image and quantify pigment of the skin, and visualize skin morphology and blood capillary landmarks. The MC-PAD detected a significant difference in the structures of some pigmented and vascular lesions of skin diseases compared with that of healthy skin ($P<0.01$). The café au lait macule (CALM) skin type was found to have a relatively higher melanin concentration and thicker stratum basale (SB) in the EP than healthy skin. The dermal vascular network of skin that had a port wine stain (PWS) had greater diameters and a denser distribution than healthy skin, as reported in clinical trials.

Conclusions: The MC-PAD has a broad range of applications for the diagnosis of human skin diseases and evaluation of the curative effect of treatments, and it can offer new perspectives in biomedical sciences.

Keywords: photoacoustic imaging; dermoscopy; *in vivo*; skin imaging; multiscale

Submitted Sep 02, 2021. Accepted for publication Jan 12, 2022.
doi: 10.21037/qims-21-878
View this article at: https://dx.doi.org/10.21037/qims-21-878

^ ORCID: 0000-0001-7936-4971.

Introduction

Medical imaging technology is of great importance in modern clinical medicine (1-4). In dermatology, detailed imaging of the structure and function of the skin is important when performing a comprehensive assessment and determining a quantitative treatment (5-7). However, despite years of advances in medical imaging technology, it has remained difficult to non-invasively visualize the structure and function of human skin with deep penetration, strong contrast, and high spatial resolution (8-10). In clinical practice, biopsies are commonly used to evaluate and analyze skin diseases (11). The technique is inherently invasive and can only provide information that is specific to a very limited portion of a lesion. Optical coherence tomography (OCT) has been used for non-invasive high-resolution imaging of the skin (2,12), but the technique still has limitations stemming from biological light scattering. Moreover, given their similar optical refractive indices, it is challenging to distinguish hair follicles, lesion vessels, sweat glands, and sebaceous glands within the dermis (13). Ultrasonography can penetrate the entire thickness of the human skin up to several centimeters (3,14); but, due to poor imaging contrast, this technique is difficult to identifying structures tens of microns below the skin surface (15). As a result, human skin diseases are often over- or under-treated.

The recent development of photoacoustic microscopy (PAM) has overcome most of the limitations of previously available techniques by integrating optical and ultrasonic imaging. It has greatly reduced the effect of tissue scattering of photons using one-way ultrasound detection while retaining a high optical absorption contrast (16-23). Successful use of PAM has been reported in numerous studies (24-35), including observations of cell distribution, monitoring of vascularization, and label-free photoacoustic (PA) angiography. However, the opto-sono objective in most PAM setups is insufficient for clinical use in dermatology given its single-scale mode (single magnification or depth of focus), which results in a poor depth of resolution and a low signal-to-noise ratio (SNR). In addition, conventional PAM imaging uses a narrow-band ultrasonic transducer, which limits the axial resolution and imaging capability of the entire system.

Although a non-focal spot can increase the penetration depth and an ultra-high frequency transducer can improve the acoustic resolution in the PAM system, high-aperture beam illumination produces discrete flares in the images, and ultra-high frequency PA signals are prone to severe attenuation and reflection in skin tissue. To address these issues, we developed a multiscale confocal photoacoustic dermoscopy (MC-PAD) system that uses a multifunction opto-sono objective that is mainly composed of a focused broadband transducer and a custom-made multiple objective lens. The core technique for high-performance multiscale imaging is the use of multiple objective lenses (typical magnifications: 4×, 10×, and 20×) and a multiscale adjustable device (focal adjustment range of 3 cm) to ensure sufficient resolution and resolve the dilated lesion vessels from several tens of microns to a few hundred microns. In addition, the multifunction opto-sono objective allows a relatively large number of photons to scatter into deeper skin tissues by selecting the appropriate magnification and focus depth position.

The human skin consists of the epidermis, dermis, and subcutaneous tissue. The epidermis includes the stratum corneum (SC) and stratum basale (SB). Numerous blood vessels are present in the dermis, and the different layers have different optical-absorption characteristics (36,37). The MC-PAD can show the epidermal structure, including the SC and SB, as well as blood vessels in the dermis, due to the strong optical absorption of melanin (the main component of SC and SB) and hemoglobin (the main component of blood vessels). Here, we demonstrate in clinical practice the multiscale imaging capability of MC-PAD from the skin epidermis to the dermis with high resolution and deep penetration. We present an effective approach for dermatological imaging via the development of a system for MC-PAD. We also present the results of our investigation into how the imaging features associated with quantification of skin pigment and port wine stain (PWS) dermatological conditions relate to pathophysiological metrics. We investigated dermal features by developing an adjustable objective with a wide range of depth of focus, with which we were able to obtain a high depth/resolution ratio for MC-PAD. Finally, we discuss how the approach can advance research into dermatological conditions, evaluate the severity of these conditions, and quantify a treatment response.

We present the following article in accordance with the Standards for Reporting Diagnostic accuracy studies (STARD) reporting checklist (available at https://qims.amegroups.com/article/view/10.21037/qims-21-878/rc).

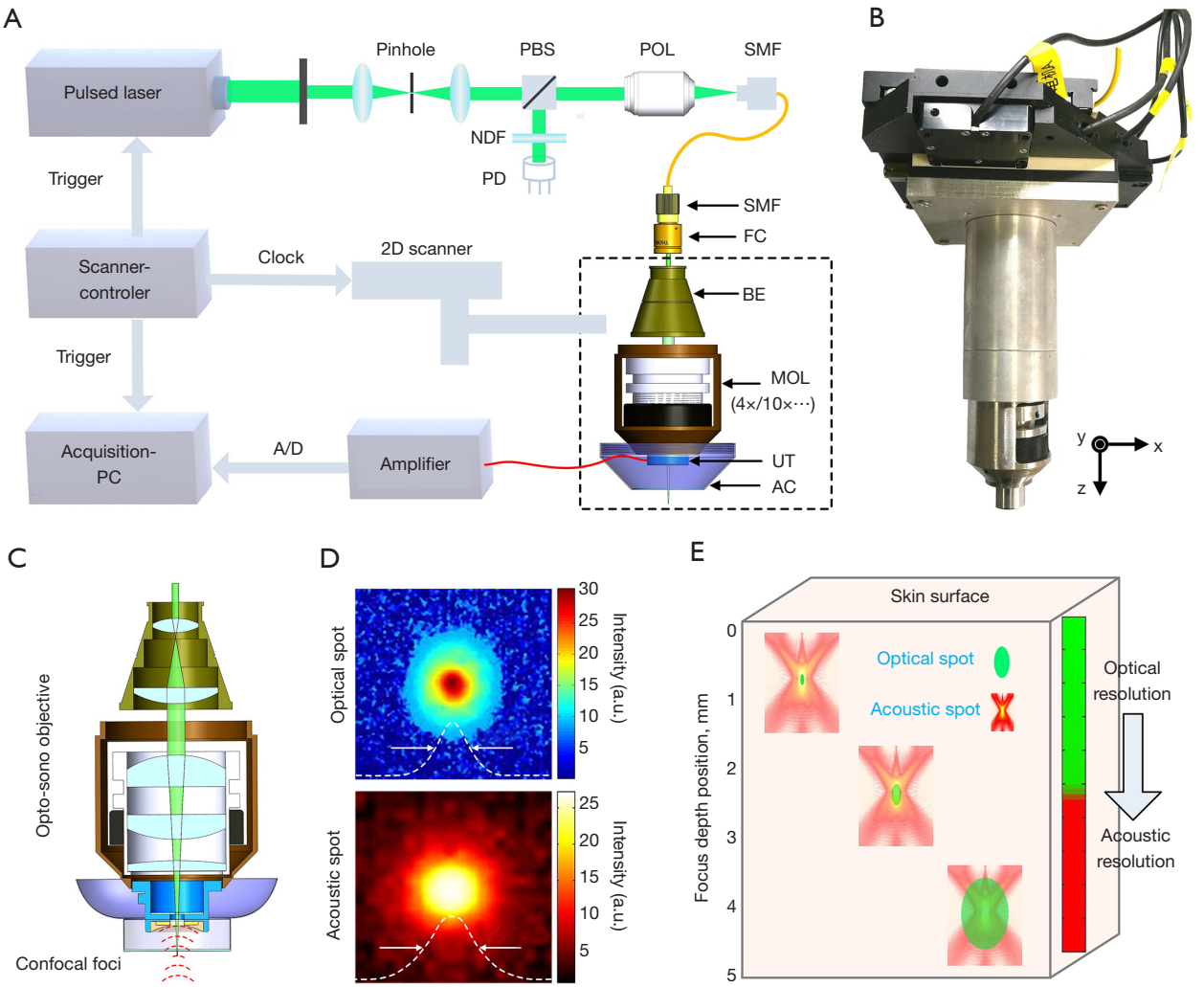

Figure 1 A schematic of the MC-PAD system. (A) A schematic of the entire setup. (B) A photograph of the opto-sono objective with a two-dimensional hollow scanner. (C) The cross-sectional structure of the opto-sono objective. (D) Intensity profiles of the optical spot and acoustic spot at the focal distance. (E) A variation diagram of system resolution as a demonstration of imaging depth. (D,E) The NA of the objective lens with 4× magnification is 0.1, and the central frequency of the ultrasound transducer is about 45 MHz. MC-PAD, multiscale confocal photoacoustic dermoscopy; NDF, neutral density filter; PBS, polarizing beam splitter; PD, photodiode; POL, plan objective lens; SMF, single-mode fiber; FC, fiber collimator; BE, beam expander (2×, 5×, and 10×); MOL, multiple objective lens; UT, ultrasound transducer; AC, adjustable coupling cup; A/D, analog to digital; NA, numerical aperture.

Methods

Bench-to-bedside translation of MC-PAD

We developed a multiscale high-resolution MC-PAD imaging system to clinically diagnose skin diseases (*Figure 1*). The detection sensitivity and SNR of the MC-PAD system can be greatly improved by the backward coaxial confocal mode (22,23). The artefacts that are induced by limited detection coverage can be avoided by using a broadband polyvinylidene fluoride (PVDF) transducer (38,39). The PVDF transducer has an overall diameter of 4 mm with a 1 mm center hole that allows the laser beam to exit. Typical focal length is 14.3 mm. The beam is generated by the spherically focused structure that produces a numerical aperture (NA) of 0.28 (the central frequency of the PVDF transducer is 45 MHz).

As shown in *Figure 1*, the system was based on a custom-made multifunction opto-sono objective and a hollow, spherically focused PVDF ultrasound transducer with a central frequency of approximately 45 MHz and large bandwidth (5–85 MHz). A 532 nm pulse laser (DTL-314QT; Laser-export Co., Ltd., Moscow, Russia) was used as the radiation source and offered sufficient contrast for skin imaging. A convex lens was used to focus the laser and pass it through a 25-μm pinhole for spatial filtering, and then the laser was focused into a single-mode fiber by a plan objective lens (with a working distance of 37.5 mm, and NA of 0.1). The laser was finally focused by the objective, and then irradiate the tested skin surface to generate ultrasonic signals. A two-dimensional scanner (range: 5×5 cm^2; scan resolution: 0.1 μm; HRXWJ-50R-2; TianRui ZhongHai, Beijing, China) was used to actuate the opto-sono objective automatically. The adjustable cup was filled with deionized water that served as an ultrasonic coupling medium. A transparent plastic film, through which light and sound could penetrate, was fixed on the head of the adjustable cup. The excitation source was eventually focused into multiple magnification modes. Those multiple magnification modes were implemented by a mechanical structure, which manually replaced independent lenses with different magnification modes, typically 4×/0.1 NA, 10×/0.3 NA, and 20×/0.55 NA. Each independent lens could be manually adjusted by the multiscale adjustable configuration from 0 to 3 cm. The beam size after passing through the collimator was about 1.5 mm, and after the beam expander it was respectively about 3, 7.5, and 15 mm for 3 expanding multiples (2×, 5×, and 10×). The adjustable cup allowed the focus of the laser beam and sound field to be under the surface of the transparent film. Each skin cross-sectional (B-scan) image was reconstructed using the collected PA signals over 0.5 mm along the *x* direction (the number of scanning points was 201) and within 0.2 s, and the spacing distance between 2 B-scan images was 0.5 mm. The duration of the entire preparation process, including placement of the imaging head on the skin surface, was about 2–3 min.

A 50 dB low-noise amplifier (LNA-650, RF BAY Inc., Gaithersburg, MD, USA) was used to sequentially pre-amplify the ultrasonic signals, which was digitized by a high-speed data acquisition device (NI5124, National Instruments Corp., Austin, TX, USA), and stored on the acquisition PCs for subsequent image reconstruction. The beam spot sizes at focus were about 3.5, 2.1, and 1.3 μm for 3 NAs (4×/0.1 NA, 10×/0.3 NA, and 20×/0.55 NA, respectively), and optical depth-of-focus was about 0.35, 0.19, 0.1 mm, respectively. The acoustic spot was about 102 μm and acoustic depth-of-focus was about 1 mm. The lateral resolution of the system with 3 objective lenses was measured by imaging a sharp-edged surgical blade, which was estimated to be 3.8, 2.3, and 1.5 μm, respectively. The axial resolution of the system depended primarily on the acoustic parameter, which was estimated to be approximately 34 μm based on the system bandwidth and acoustic speed within the tissue. The maximum field of view in the case of each magnification depended on the motor's scanning range, which was about 5×5 cm^2 at most.

To conform to the American National Standards Institute safety limit (20 mJ/cm^2) (40), the energy density of the laser beam on the tissue surface was about 10 mJ/cm^2. The study was conducted in accordance with the Declaration of Helsinki (as revised in 2013). The study was approved by the Ethics Committee of the First Medical Center of People's Liberation Army (PLA) General Hospital (Clinical Trials. gov number, 2017 Ethic Review No. 012). Before skin imaging was performed, written informed consent was provided by all individual participants.

Implications of scalable adjustment in MC-PAD skin imaging

The position of the adjustable confocal opto-sono objective could be varied in order to shift the location of the acoustic and optical focuses with respect to the skin surface, so the resolution and imaging depth of the MC-PAD system can be switched in a flexible manner (*Figure 2A*). The amplitude of PA signals at different depths was presented in the same healthy opisthenar skin, and the penetration depth of skin for the PAD system was approximately 1.8 mm, as shown in *Figure 2B*. Due to the scattering properties of the skin, the SNR of the system deteriorated as imaging depth increased. Additionally, to obtain a greater imaging depth (≥3 mm), the use of a near-infrared light may be feasible. To study the influence of different NA modes on the imaging performance, the PA B-scan images of palmar skin were obtained to be reconstructed by those NA modes (4×/0.1, 10×/0.3, and 20×/0.55) with the same laser energy and focusing depth as shown in *Figure 2C*. The results showed that the high NA mode allowed for the rendering of fine spatial details but with reduced imaging depth, whereas the low NA mode allowed for fine

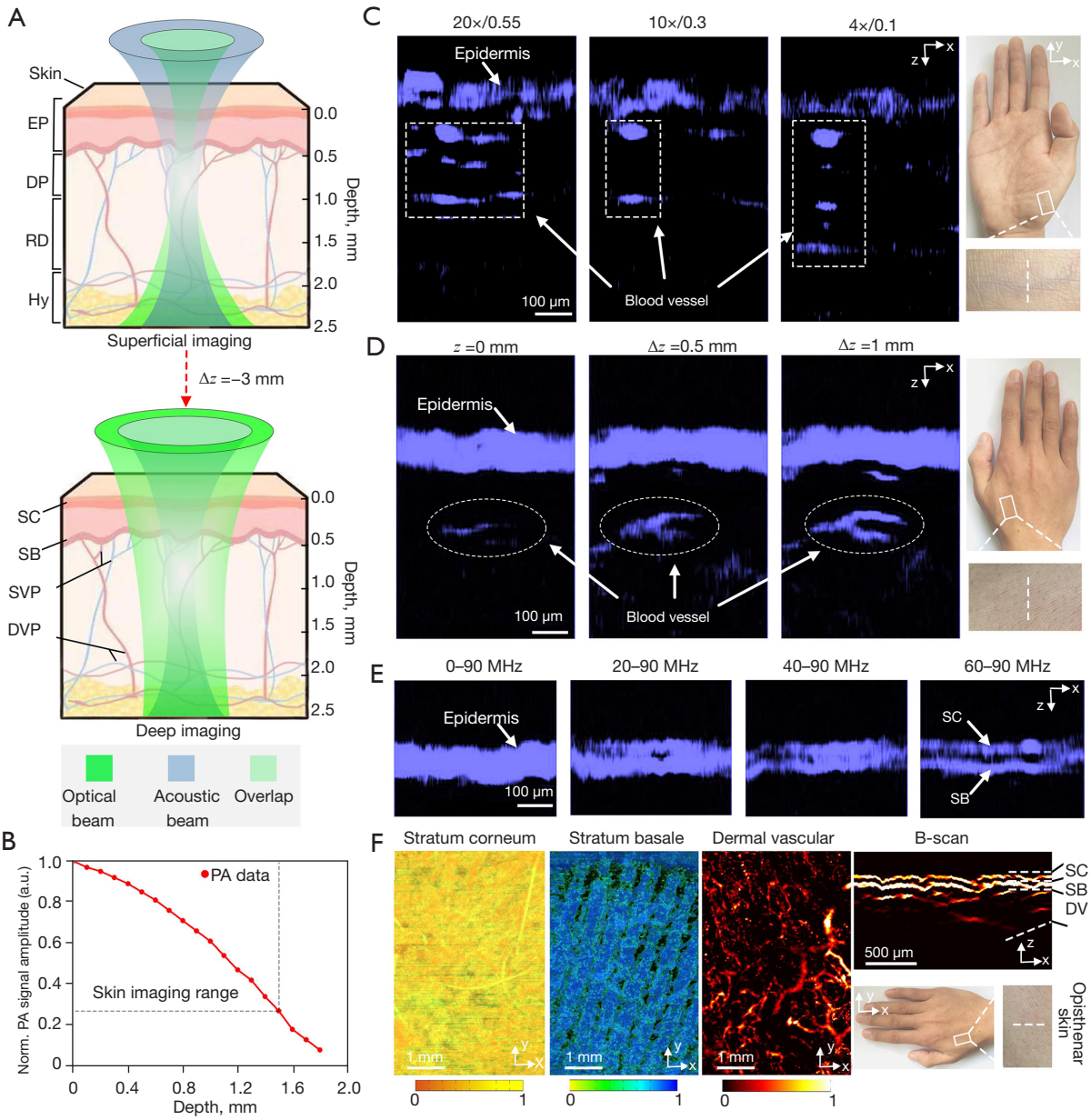

Figure 2 Skin imaging with the MC-PAD system. (A) A schematic of optical excitation and photoacoustic (PA) signal generation by multilayered structures of the skin for different imaging depths. The position of the adjustable confocal opto-sono objective can be varied to shift the location of the acoustic and optical focuses with respect to the skin surface, so the different imaging depths of the MC-PAD system can be switched in a flexible manner. The d_z is the axial distance by which the optical focus moves. (B) PA signal amplitude at different imaging depths. (C) Cross-sectional PA images of palm skin at three numerical aperture (NA) modes (4×/0.1, 10×/0.3, and 20×/0.55). (D) Cross-sectional PA images of opisthenar skin at different focusing depths (NA, 4×/0.1). (E) Cross-sectional PA images of epidermis at different frequency bands (NA, 4×/0.1). (F) MC-PAD images of the opisthenar skin. PA images [from left to right: volume-rendered images of SC and SB, and MIP images of skin dermal vascular (DV)] displayed along the direction perpendicular to the skin surface within the limits marked in PA B-scan section. Each color bar represents normalized PA amplitude. MC-PAD, MC-PAD, multiscale confocal photoacoustic dermoscopy; EP, epidermis; DP, dermal papillae; RD, reticular dermis; Hy, hypodermis; SC, stratum corneum; SB, stratum basale; SVP, superficial vascular plexus; DVP, deep vascular plexus; MIP, maximum intensity projection.

control of imaging depth but with reduced resolution of skin structures. We then reconstructed cross-sectional PA images of the opisthenar skin at different focusing depths (~500 μm between PA images) with the same laser energy and NA mode (4×/0.1) as shown in *Figure 2D*. The results showed that this multiscale adjustable structure allowed visualization of more vascular details that other imaging techniques and demonstrated the ability of the MC-PAD to provide enhanced structural details of the microvasculature by the focal adjustment. Subsequently, detected PA signals of the opisthenar skin were reconstructed and separated into different frequency bands, typically 5–90, 20–90, 40–90, and 60–90 MHz, and the images with the different frequency bands were reconstructed (*Figure 2E*). This operation provided sufficient axial resolution to separate SC from SB using the broadband PVDF transducer. The imaging of SC, SB, and dermal vascular tissue was obtained using 20×/0.55 NA, 10×/0.3 NA, and 4×/0.1 NA, respectively. To better display the skin information, images needed to take up a larger size range, as shown in *Figure 2F*, than those in *Figure 2C-2E*. Consequently, *Figure 2F* shows noninvasive PA imaging of dermal vasculature, skin layers, and capillary loops at a level of detail and a resolution-to-depth ratio (approximately 0.006) that has not been achieved by other modalities. Therefore, the combination of NA modes, focusing depths, and frequency equalization has powerful capabilities that can improve skin imaging techniques.

Results

MC-PAD of cells in vivo, characteristic extraction, and identification

This study was performed to investigate whether MC-PAD with the 20×/0.55 NA mode could be used to identify specific cells. The corresponding PA signal intensities of red blood cells (RBCs) and murine melanoma B16F10 cells were measured. Upon 532 nm laser beam illumination, both RBCs and melanoma cells generated marked PA signals, but the PA intensity of melanoma cells was approximately 1.63 times greater than that of the RBCs at 532 nm (*Figure 3A*) (24). Therefore, PA signal intensity was extracted as a parameter to recognize RBCs and melanoma cells. To confirm whether cell diameter was another characteristic that discerns RBCs from melanoma cells, cell diameters were measured *in vitro* (*Figure 3B*,*3C*). Meanwhile, to verify that MC-PAD could be used to detect specific cells *in vivo*, metastatic cells were imitated using B16F10 cells suspended in a 100 μL saline solution and injected into the circulatory system of mice via the tail vein. Cells were then subjected to MC-PAD monitoring in an ear vein. A microvasculature image of an area at the mouse ear edge (*Figure 3D*) was scanned at 2-μm intervals. Then, 1 appropriate blood vessel was chosen for the obtainment of measurements. The vessel was 15 μm in diameter. The system was employed in the fast repetitive B-scan mode. The scanning lines, labelled x, were perpendicular to the selected blood vessel and set to 30 μm in 20 steps. The B-scan time series cumulating images are presented in *Figure 3E* at one point. In the x-t image, RBCs were circular and flowed one after another, which was consistent with the one-dimensional scanning PA signal shown in *Figure 3A*.

Identification analysis of RBCs and melanoma cells was performed (*Figure 3F*). However, the diameter of RBCs can vary depending on maturity (for example, immature RBCs are larger) and disease, and the size of cancer cells, including melanoma, can also vary, so that cell diameter alone may not be sufficient to identify different cell types. To precisely distinguish between different kinds of cells, another parameter, $\Gamma = P \times D$, was incorporated according to the maximum PA intensity (P) and cell diameter (D) into a pattern and an identification strategy (*Figure 3G*). The detection accuracy of *in vivo* PA flow cytography of the Γ characteristic was markedly better than that of other characteristics.

MC-PAD of skin epidermal pigment: measurement and quantification

The deepest layer of the epidermis is the SB, which is the upper part of the epidermal-dermal junction (EDJ). The SB contains a large number of melanocytes and melanin particles that form a layer of pigment with strong optical absorption. Thus, the SB can be separated from the SC and EDJ because of its spatial location and strong optical absorption. In the study group, MC-PAD images were examined for epidermal pigment (melanin content) alterations of café au lait macule (CALM) skin. The parameters computed were the thickness of the SB and epidermis and the PA signal intensity (which has a linear relationship with the melanin concentration) in the epidermis (41). These measurements were used as label-free

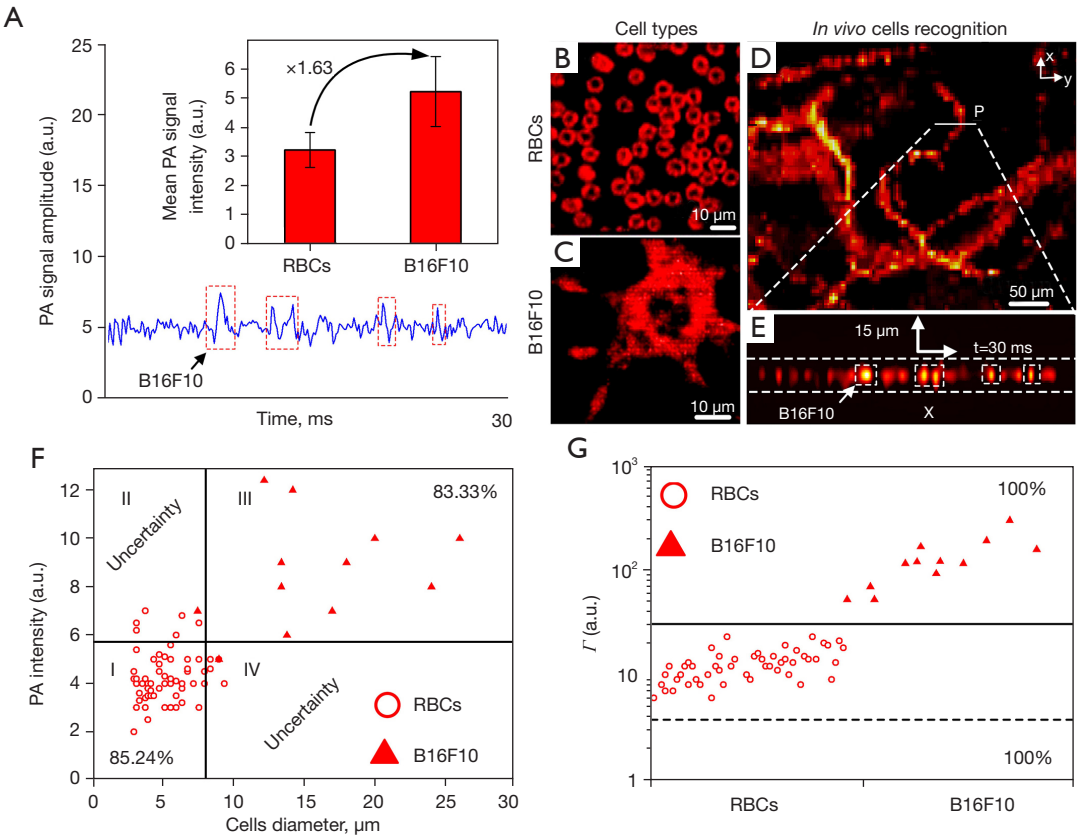

Figure 3 *In vivo* recognition of RBCs and murine melanoma B16F10 cells. (A) One-dimensional scanning PA capillary cytometry. PA detection of single B16F10 cells, and the corresponding PA signal intensities at 532 nm. (B,C) PA images of RBCs and melanoma B16F10 cells. The scanning interval was 1 μm. (D) Superficial microvasculature PA image in a mouse ear. The scanning interval was 1 μm and scan points were 1,000×1,000. (E) A B-scan *x*-*t* image of cells in the vessel labelled *p* in (D). (F) A scatter plot of cell long diameter and PA intensity. (G) A scatter plot of the Γ parameters of cells (defined as $\Gamma = P \times D$, where P is the maximum PA intensity of the measured cell and D is the cell diameter). These cell diameters were measured using the software Image J. RBCs, red blood cells; PA, photoacoustic.

biomarkers corresponding to the melanin content of the skin. The pigmentation of CALM skin is mainly distributed in SB that generally has a thickness greater than 60 μm (42). To achieve good resolution with sufficient penetration of the lesion epidermis, the 10× magnification mode was used to image CALM skin in clinical trials.

The MC-PAD images containing corresponding PA B-scan images of healthy skin and CALM skin from one Asiatic volunteer with CALM skin are shown in *Figure 4A*,*4B*. In addition, *Figure 4C*,*4D* show three-dimensional (3D) PA epidermal volumetric images, and volume-rendered images of the SB and SC of healthy skin and CALM skin from the same patient, respectively. The blue part in the 3D PA epidermal volumetric images represents the melanin component of the epidermal layer, which was greater in CALM skin.

We recruited 5 Asiatic volunteers with CALM skin for the acquisition of PA images by MC-PAD. In total, 60 scanning positions from independent skin regions of the 5 volunteers (n=30 CALM skin; n=30 healthy skin) were obtained. The results of the PA signal intensities indicated that the CALM skin had a higher PA signal intensity than that of healthy skin, as shown in *Figure 4E*. In addition, the PA signal intensities (melanin concentration) and SB thickness from the patient were counted and presented in *Figure 4F*, which shows that the CALM skin had a significantly thicker SB and higher melanin concentration than the healthy skin, demonstrating that MC-PAD can

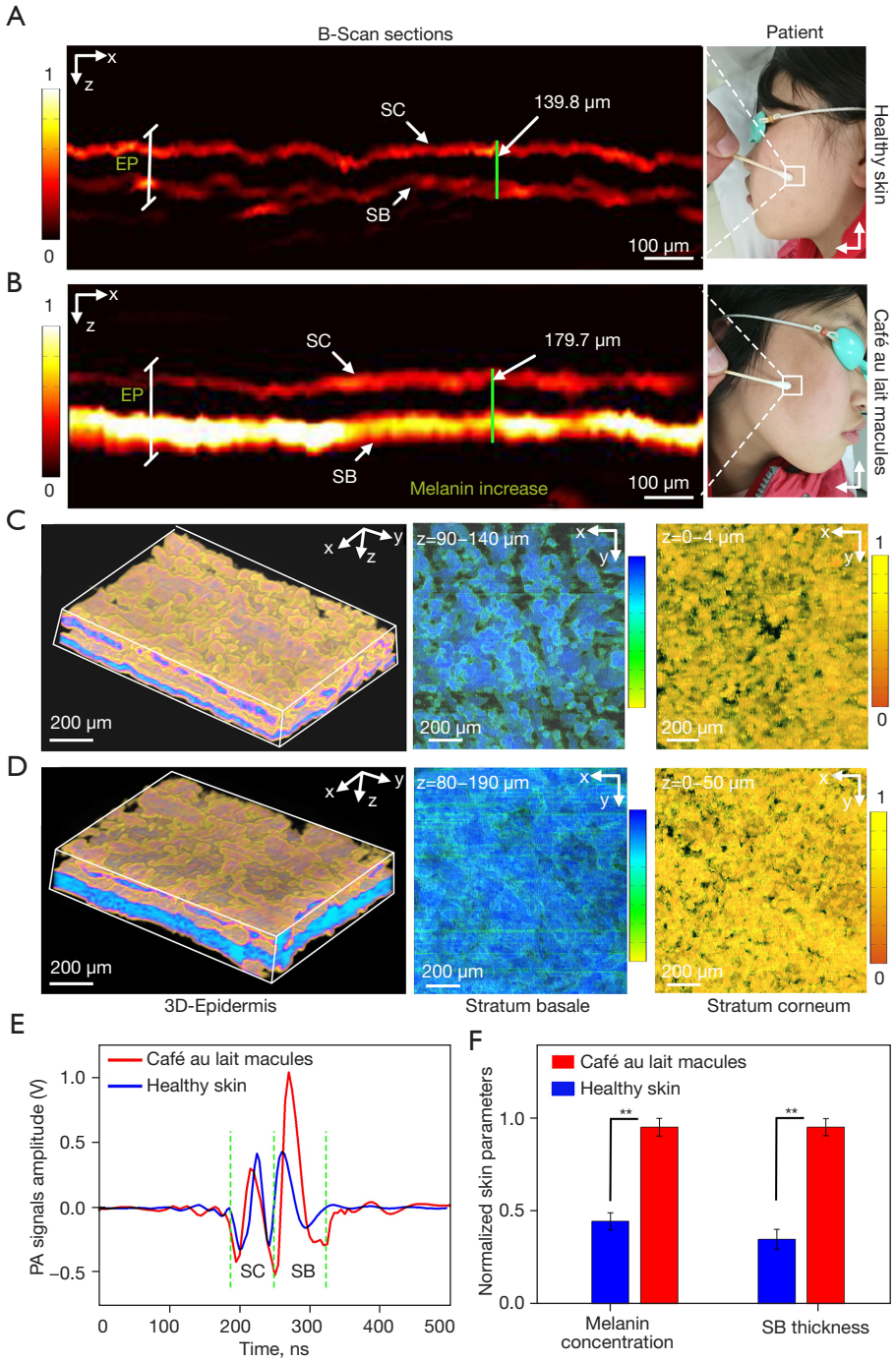

Figure 4 Comparison of *in vivo* contrasts from healthy skin and CALM skin by MC-PAD. (A,B) PA images of healthy and CALM skins from one Asiatic volunteer with CALM skin and corresponding photographs (white boxes indicate detection areas). (C,D) Three-dimensional PA volumetric images of the EP, and volume-rendered images of SB and SC from healthy skin and CALM skin of the patient. SB (blue) can be clearly distinguished from SC (yellow) below the surface at a depth of 70–210 μm. (E) PA amplitude profiles along epidermal depth direction of healthy skin and CALM skin from the patient. (F) Statistics, i.e., average melanin concentration and SB thickness of healthy skin and CALM skin of the patient (**, P<0.01; mean ± SD). Each color bar represents normalized PA amplitude. CALM, café au lait macule; MC-PAD, multiscale confocal photoacoustic dermoscopy; PA, photoacoustic; EP, epidermis; SB, stratum basale; SC, stratum corneum; SD, standard deviation.

clearly reveal fine structures of SC and SB. Therefore, MC-PAD can non-destructively and quantitatively reveal that CALM skin has a relatively higher melanin concentration and thicker SB in the epidermis than healthy skin and can be extended to assess a larger spectrum of conditions of pigmented dermatoses, such as pigmented nevi.

MC-PAD of healthy skin versus contralateral PWS skin in individuals

We then investigated whether MC-PAD could be used to analyze and quantify the vascular features of PWS skin. The PWS skin lesion vessels are mainly distributed in the superficial layer of the dermis, and generally have a diameter greater than 40 μm (43). To obtain high spatial resolution with sufficient imaging depth of dilated PWS vessels, the 4×/0.1 mode of MC-PAD was used to image the skin lesions. We imaged areas of healthy skin measuring 3 mm × 3 mm from one PWS patient, which revealed marked changes compared with skin affected by PWS (*Figure 5A*). The elongated and dilated capillary loops of PWS skin were visualized in red via hemoglobin absorption. Detection areas A1–A6 from 6 Asiatic volunteers with PWS skin were used to acquire PA images by MC-PAD. In total, 60 scanning positions from independent regions of the 6 volunteers (n=30 PWS skin; n=30 healthy skin) were obtained. The difference in microvessel density in healthy and PWS skin was defined as $\rho = S/N$, where ρ was microvessel density, S was relative microvessel area (the ratio of the actual microvessel area to the imaging area of system), and N is the number of microvessels). The results showed that dermal vessels had greater diameters and were denser in appearance in PWS skin than in healthy skin (*Figure 5B*). These results are consistent with the histology of PWS skin (37, 43).

Cross-sectional MC-PAD images of another PWS patient were compared with OCT cross-sections for the same areas of skin (*Figure 5C*). The OCT cross-sections confirmed the capillary elongation and increased dermal vascularization that had been visualized by the MC-PAD. Quantitative comparison of the superficial lesion vessels that were observed in the MC-PAD and OCT images showed a good correlation between the 2 methods, and both showed increased vascularization of the dermis, but MC-PAD offered a deeper imaging depth. Therefore, MC-PAD offers a distinct depth advantage over OCT in the diagnosis of PWS.

Conclusions

The MC-PAD system used multiple objective lenses, a multiscale adjustable configuration, a wide-bandwidth PVDF transducer, tomographic reconstruction, and high NA data collection, which offered an approach to identify and distinguish the characteristics of different types of cells (*Figure 3)*. This approach could also measure and quantify skin pigment (*Figure 4*) and visualize and materialize skin morphology and blood capillary landmarks (*Figure 5*). Overall, the MC-PAD can discern cell types based on their intrinsic characteristics, including shape, size, and signal intensity. It can also detect the abnormal plexus of the dilated melanin layer located in the pigmented skin, enable quantification of the volume, concentration, and thickness of melanin, and assess visualization of skin abnormalities. Therefore, the MC-PAD system could have high clinical potential in analysis, monitoring, and treatment planning for skin disorders.

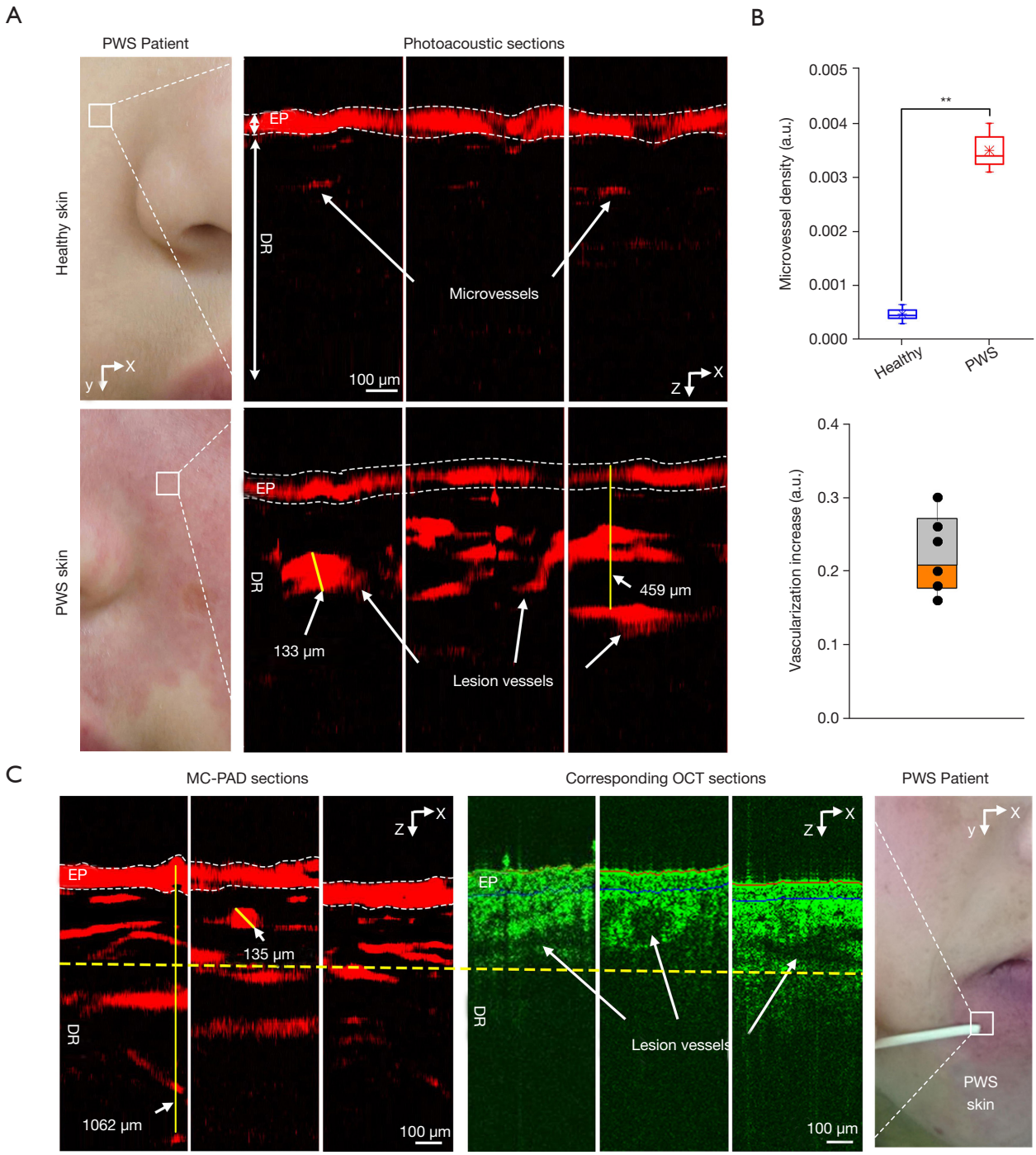

Figure 5 MC-PAD of healthy skin versus contralateral PWS skin. (A) Photographs of the skin of one patient with PWS (white boxes indicate the detection areas) and corresponding photoacoustic images. The images depict 3 consecutive cross-section photoacoustic maps along the x-axis, in which the EP is denoted with white dotted lines. Below the EP, a dilated and dense vascular structure of the dermis is resolved (in red). (B) Box-and-whisker plots of the differences between measurements for PWS and healthy skin (**, P<0.01). The orange and grey parts correspond to values from the median to the third quartile and the median to the first quartile, respectively. (C) MC-PAD cross-sectional images (left) and corresponding OCT cross-sectional images (right) from PWS skin of another patient. MC-PAD, multiscale confocal photoacoustic dermoscopy; PWS, port wine stain; EP, epidermis; OCT, optical coherence tomography.

Acknowledgments

Funding: This research was supported by the National Natural Science Foundation of China (Nos. 61835015, 61635014), Guangdong Basic and Applied Basic Research Foundation (No. 2020A1515110758), and Fundamental Research Funds for the Central University (No. 31020200QD040).

Footnote

Reporting Checklist: The authors have completed the Standards for Reporting Diagnostic accuracy studies (STARD) reporting checklist. Available at https://qims.amegroups.com/article/view/10.21037/qims-21-878/rc

Conflicts of Interest: All authors have completed the ICMJE uniform disclosure form (available at https://qims.amegroups.com/article/view/10.21037/qims-21-878/coif). The authors have no conflicts of interest to declare.

Ethical Statement: The authors are accountable for all aspects of the work in ensuring that questions related to the accuracy or integrity of any part of the work are appropriately investigated and resolved. The study was conducted in accordance with the Declaration of Helsinki (as revised in 2013). The study was approved by the Ethics Committee of the First Medical Center of PLA General Hospital (Clinical Trials. gov number, 2017 Ethic Review No. 012). Before skin imaging was undertaken, written informed consent was provided by all participants.

References

1. Sipkins DA, Wei X, Wu JW, Runnels JM, Côté D, Means TK, Luster AD, Scadden DT, Lin CP. In vivo imaging of specialized bone marrow endothelial microdomains for tumour engraftment. Nature 2005;435:969-73.
2. Deegan AJ, Lu J, Sharma R, Mandell SP, Wang RK. Imaging human skin autograft integration with optical coherence tomography. Quant Imaging Med Surg 2021;11:784-96.
3. Demené C, Robin J, Dizeux A, Heiles B, Pernot M, Tanter M, Perren F. Transcranial ultrafast ultrasound localization microscopy of brain vasculature in patients. Nat Biomed Eng 2021;5:219-28.
4. Wang X, Pang Y, Ku G, Xie X, Stoica G, Wang LV. Noninvasive laser-induced photoacoustic tomography for structural and functional in vivo imaging of the brain. Nat Biotechnol 2003;21:803-6.
5. Berardesca E, Maibach H, Wilhelm K. editors. Noninvasive diagnostic techniques in clinical dermatology. Springer Science & Business Media, 2013.
6. Kittler H, Pehamberger H, Wolff K, Binder M. Diagnostic accuracy of dermoscopy. Lancet Oncol 2002;3:159-65.
7. Rocha L, Menzies SW, Lo S, Avramidis M, Khoury R, Jackett L, Guitera P. Analysis of an electrical impedance spectroscopy system in short-term digital dermoscopy imaging of melanocytic lesions. Br J Dermatol 2017;177:1432-8.
8. Appel AA, Anastasio MA, Larson JC, Brey EM. Imaging challenges in biomaterials and tissue engineering. Biomaterials 2013;34:6615-30.
9. De Backer D, Ospina-Tascon G, Salgado D, Favory R, Creteur J, Vincent JL. Monitoring the microcirculation in the critically ill patient: current methods and future approaches. Intensive Care Med 2010;36:1813-25.
10. Roustit M, Cracowski JL. Non-invasive assessment of skin microvascular function in humans: an insight into methods. Microcirculation 2012;19:47-64.
11. Yu W, Ma G, Qiu Y, Chen H, Jin Y, Yang X, Hu X, Wang T, Chang L, Zhou H, Li W, Lin X. Why do port-wine stains (PWS) on the lateral face respond better to pulsed dye laser (PDL) than those located on the central face? J Am Acad Dermatol 2016;74:527-35.
12. Latrive A, Teixeira LR, Gomes AS, Zezell DM. Characterization of skin Port-Wine Stain and Hemangioma vascular lesions using Doppler OCT. Skin Res Technol 2016;22:223-9.
13. Wang LV, Wu H. Biomedical Optics: Principles and Imaging. Wiley: Hoboken, 2007.
14. Gutierrez M, Wortsman X, Filippucci E, De Angelis R, Filosa G, Grassi W. High-frequency sonography in the evaluation of psoriasis: nail and skin involvement. J Ultrasound Med 2009;28:1569-74.
15. Jasaitiene D, Valiukeviciene S, Linkeviciute G, Raisutis

R, Jasiuniene E, Kazys R. Principles of high-frequency ultrasonography for investigation of skin pathology. J Eur Acad Dermatol Venereol 2011;25:375-82.
16. Zhong H, Jiang D, Lan H, Duan T, Gao F, Gao F. Low-Cost Multi-Wavelength Photoacoustic Imaging Based on Portable Continuous-Wave Laser Diode Module. IEEE Trans Biomed Circuits Syst 2020;14:738-45.
17. Liu C, Liang Y, Wang L. Single-shot photoacoustic microscopy of hemoglobin concentration, oxygen saturation, and blood flow in sub-microseconds. Photoacoustics 2019;17:100156.
18. Estrada H, Rebling J, Hofmann U, Razansky D. Discerning calvarian microvascular networks by combined optoacoustic ultrasound microscopy. Photoacoustics 2020;19:100178.
19. Conkey DB, Caravaca-Aguirre AM, Dove JD, Ju H, Murray TW, Piestun R. Super-resolution photoacoustic imaging through a scattering wall. Nat Commun 2015;6:7902.
20. Kim H, Baik JW, Jeon S, Kim JY, Kim C. PAExM: label-free hyper-resolution photoacoustic expansion microscopy. Opt Lett 2020;45:6755-8.
21. Wang Z, Yang F, Cheng Z, Zhang W, Xiong K, Yang S. Photoacoustic-guided photothermal therapy by mapping of tumor microvasculature and nanoparticle. Nanophotonics 2021;10:3359-68.
22. Cheng Z, Ma H, Wang Z, Yang S. In vivo volumetric monitoring of revascularization of traumatized skin using extended depth-of-field photoacoustic microscopy. Frontiers of Optoelectronics 2020;13:307-17.
23. Ma H, Yang S, Cheng Z, Xing D. Photoacoustic confocal dermoscope with a waterless coupling and impedance matching opto-sono probe. Opt Lett 2017;42:2342-5.
24. He G, Xu D, Qin H, Yang S, Xing D. In vivo cell characteristic extraction and identification by photoacoustic flow cytography. Biomed Opt Express 2015;6:3748-56.
25. Ning B, Kennedy MJ, Dixon AJ, Sun N, Cao R, Soetikno BT, Chen R, Zhou Q, Kirk Shung K, Hossack JA, Hu S. Simultaneous photoacoustic microscopy of microvascular anatomy, oxygen saturation, and blood flow. Opt Lett 2015;40:910-3.
26. Aguirre J, Schwarz M, Garzorz N, Omar M, Buehler A, Eyerich K, Ntziachristos V. Precision assessment of label-free psoriasis biomarkers with ultra-broadband optoacoustic mesoscopy. Nat Biomed Eng 2017;1:0068.
27. Wang Z, Yang F, Ma H, Cheng Z, Yang S. Photoacoustic and ultrasound (PAUS) dermoscope with high sensitivity and penetration depth by using a bimorph transducer. J Biophotonics 2020;13:e202000145.
28. Ma H, Cheng Z, Wang Z, Zhang W, Yang S. Switchable optical and acoustic resolution photoacoustic dermoscope dedicated into in vivo biopsy-like of human skin. Appl Phys Lett 2020;116:073703.
29. Zhang HF, Maslov K, Wang LV. In vivo imaging of subcutaneous structures using functional photoacoustic microscopy. Nat Protoc 2007;2:797-804.
30. Seeger M, Soliman D, Aguirre J, Diot G, Wierzbowski J, Ntziachristos V. Pushing the boundaries of optoacoustic microscopy by total impulse response characterization. Nat Commun 2020;11:2910.
31. Qin W, Gan Q, Yang L, Wang Y, Qi W, Ke B, Xi L. High-resolution in vivo imaging of rhesus cerebral cortex with ultrafast portable photoacoustic microscopy. Neuroimage 2021;238:118260.
32. Yang J, Wu D, Tang Y, Jiang H. Photoacoustic microscopy of electronic acupuncture (EA) effect in small animals. J Biophotonics 2017;10:217-23.
33. Vienneau E, Vu T, Yao J. Photoacoustic Imaging of Skin. In: Xu C, Wang X, Pramanik M. editiors. Imaging Technologies and Transdermal Delivery in Skin Disorders. Wiley, 2019:411-42.
34. Deán-Ben XL, Razansky D. Optoacoustic imaging of the skin. Exp Dermatol 2021;30:1598-609.
35. Deán-Ben XL, López-Schier H, Razansky D. Optoacoustic micro-tomography at 100 volumes per second. Sci Rep 2017;7:6850.
36. Lu H, Edwards C, Gaskell S, Pearse A, Marks R. Melanin content and distribution in the surface corneocyte with skin phototypes. Br J Dermatol 1996;135:263-7.
37. Xu D, Yang S, Wang Y, Gu Y, Xing D. Noninvasive and high-resolving photoacoustic dermoscopy of human skin. Biomed Opt Express 2016;7:2095-102.
38. Kelley T, Hutchings K, Jenkinson M, Dawson I, Krawec K, Miyagawa PS, Kern JH, Edge R. In situ monitoring of PVDF ultrasound transducers under gamma irradiation. Nondestruct Test Eval 2020;35:207-21.
39. Pullano SA, Critello CD, Bianco MG, Menniti M, Fiorillo AS. PVDF Ultrasonic Sensors for In-Air Applications: A Review. IEEE Trans Ultrason Ferroelectr Freq Control 2021;68:2324-35.
40. American National Standard for Safe Use of Lasers. Laser Institute of America, ANSI Z136.1-2014, 2014.
41. Ma H, Cheng Z, Wang Z, Gu Y, Zhang T, Qiu H, Yang S. Fast linear confocal scanning photoacoustic dermoscopy for non-invasive assessment of chromatodermatosis. Appl Phy Lett 2018;113:083704.

42. De Schepper S, Boucneau J, Vander Haeghen Y, Messiaen L, Naeyaert JM, Lambert J. Café-au-lait spots in neurofibromatosis type 1 and in healthy control individuals: hyperpigmentation of a different kind? Arch Dermatol Res 2006;297:439-49.

43. Smithies DJ, van Gemert MJ, Hansen MK, Milner TE, Nelson JS. Three-dimensional reconstruction of port wine stain vascular anatomy from serial histological sections. Phys Med Biol 1997;42:1843-7.

Cite this article as: Ma H, Wang Z, Cheng Z, He G, Feng T, Zuo C, Qiu H. Multiscale confocal photoacoustic dermoscopy to evaluate skin health. Quant Imaging Med Surg 2022;12(5):2696-2708. doi: 10.21037/qims-21-878

